Chemical Engineering Journal 490 (2024) 151651

Contents lists available at ScienceDirect

Chemical Engineering Journal

journal homepage: www.elsevier.com/locate/cej

Hollow fiber gas-diffusion electrodes with tailored crystal facets for tuning syngas production in electrochemical CO_2 reduction

Guoliang Chen [a], Lei Ge [a,b,*], Yizhu Kuang [a], Hesamoddin Rabiee [a,c,*], Beibei Ma [c], Fatereh Dorosti [c], Ashok Kumar Nanjundan [a,b], Zhonghua Zhu [c], Hao Wang [a,b,*]

[a] Centre for Future Materials, University of Southern Queensland, Springfield, QLD 4300, Australia
[b] School of Engineering, University of Southern Queensland, Springfield, QLD 4300, Australia
[c] School of Chemical Engineering, The University of Queensland, Brisbane, QLD 4072, Australia

ARTICLE INFO

Keywords:
Electrochemical reduction of CO_2
Hollow fiber gas diffusion electrode
Electrocatalyst with tailored crystal facet
Syngas production

ABSTRACT

Electrochemical reduction of CO_2 (CO_2RR) in aqueous electrolytes not only relies on advanced gas diffusion electrodes (GDEs) to improve CO_2 mass transportation but also efficient electrocatalysts to produce specific products. Herein, to produce syngas (CO and H_2 mixture), a facet-orientated zinc nanosheet catalyst was electrodeposited on the Cu hollow fiber GDE via a controllable facile surfactant-assisted method. The introduction of cationic surfactant cetyl trimethyl ammonium bromide (CTAB) could manipulate the nucleation and crystal growth of zinc ions around the GDE during the electrodeposition process, leading to controlled changes in the surface free energy and tuned zinc crystal growth orientation. Consequently, the ZncNS-HF with the largest ratio of Zn (101)/Zn (002), resulted in a high current density of 73.3 mA/cm^2 and a high syngas production rate of 1328.6 μmol/h•cm^2 at applied potential −1.3 V (vs. RHE). This comes from the hierarchical structure of HFGDE, which provides sufficient CO_2 reaching the catalyst/electrolyte interface, and the well-connected zinc nanosheets contribute to a significant number of active sites for CO_2RR. This is the first time to configure flow-through or gas-penetrated HFGDEs with zinc crystal facets controlled nanosheet catalysts for syngas production. This research demonstrates the high potential of nanoengineering catalysts for HFGDEs to achieve high production rates of syngas.

1. Introduction

Electrochemical reduction of CO_2 (CO_2RR) has been redeemed as an effective way to mitigate the negative impact (i.e., climate change) of carbon emissions while storing renewable electricity in the form of chemical stocks [1–3]. The CO_2RR can be efficiently conducted at ambient conditions to produce various value-added products, for example, syngas (H_2 and CO mixture), methane, ethylene, formate, ethanol, and other C_{2+} products [4–9]. In particular, syngas can be further utilized as an important chemical feedstock for methanol synthesis (CO/H_2 ratio of 0.5), syngas fermentation (CO/H_2 ratio of 1 to 3.33), and Fischer-Tropsch synthesis (CO/H_2 ratio of 1.67) [10–13]. The tunability of the CO/H_2 ratio via CO_2RR provides numerous opportunities to synthesise different products through the above reactions. It is also more economical to directly use syngas for chemical synthesis via existing mature industrial techniques, compared to using low-concentration CO_2RR liquid products which require energy-intensive separation from the aqueous electrolytes [14]. However, improving syngas yield and getting a suitable ratio of CO/H_2 still requires tremendous work via the rational design of both electrodes and electrocatalysts.

The electrode configuration plays a vital role in regulating CO_2 gas accessibility and mass transport to determine CO_2RR performance. For planar electrodes, the low CO_2 solubility in aqueous electrolytes and the long distance of CO_2 transportation from bulk electrolytes to active sites result in a sluggish reaction kinetic and a low current density [15,16]. To address this issue, the integration of gas diffusion electrodes (GDEs) and flow cells or membrane electrode assemblies can promote the fast diffusion of CO_2 to the active sites, thus enabling the reaction to operate at an industrial-scale current (>200 mA/cm^2) [17–20]. However, the complexity of assembling a planar GDE consisting of a catalyst layer, a microporous, and a super hydrophobic macroporous layer for gas diffusion, the flooding issue, and long-time operation stability limit its potential for industrial applications [21,22]. Promisingly, the

* Corresponding authors at: Centre for Future Materials, University of Southern Queensland, Springfield, QLD 4300, Australia.
E-mail addresses: lei.ge@usq.edu.au (L. Ge), h.rabiee@uq.edu.au (H. Rabiee), hao.wang@usq.edu.au (H. Wang).

https://doi.org/10.1016/j.cej.2024.151651
Received 13 February 2024; Received in revised form 5 April 2024; Accepted 24 April 2024
Available online 24 April 2024

configuration of hollow fiber gas diffusion electrodes (HFGDEs) can reduce conventional GDE assembling complexity due to its self-supported metal porous structures [21,23–27]. The fabrication of HFGDEs can be carried out in a facile dry-wet extrusion process, and a hundred meters of green fiber can be produced in one batch, showing a high potential for large-scale manufacture [24,27]. It is also feasible to scale up HF-type electrodes by making HF-lined or circled arrays for industrial applications [28]. The HFGDE enables CO_2 gas to build up pressure in the lumen side of the fiber to penetrate through the tubular walls, providing sufficient CO_2 to enhance gas-electrolytes-catalysts triple phase reactions, which facilitates the achievement of industry-level current density. Cu-based HFGDE was first used by Kas, and the production of CO was at least one magnitude larger than nanocrystalline Cu electrodes [23]. Chen fabricated Cu (1 0 0)-rich Cu hollow fiber achieved a FE C_{2+} of 62.8 % and a current density of 2.3 A/cm^2, demonstrating the high potential for achieving industry-level current density [28].

Nanoengineering electrocatalyst is one the most effective methods to determine the CO_2RR reaction path and product selectivity [29,30]. To produce syngas, a dual-active-site catalyst is required to promote both hydrogen evolution reaction (HER) and electrocatalytic CO_2 to CO conversion. Combining noble metals (i.e., Au, Ag) and transition metals (i.e., Fe, Co, Ni) can be effective in producing varying ratios of syngas [31,32]. The noble metal can act as a CO active site, while the transition metal favors HER. Moreover, controlling the active sites when designing a single-atom catalyst can also help regulate the ratio of CO/H_2 [33,34]. A Ni-Co double single-atom catalyst was developed to produce syngas, and the CO/H_2 ratio range of 0.23 to 2.26 was achieved by adjusting the Ni/Co molar ratio [35]. The facet control of metal or metal oxide electrocatalysts can be another facile way to tune the syngas ratio. For instance, zinc catalyst can be a suitable candidate to produce syngas by regulating the ratio of the Zn (1 0 1) to Zn (0 0 2) facet [36]. The Zn (1 0 1) facet is preferred for CO production, and the Zn (0 0 2) facet contributes to HER. The Zn (1 0 1) facet has a lower energy barrier towards CO_2RR and a higher energy barrier towards HER than the Zn (0 0 2) facet [37,38]. In our previous work, we successfully electrodeposited Sn and Bi catalysts into Cu-based HFGDEs for electrocatalytic conversion of CO_2 to formic acid [39–42]. The asymmetric Cu-based HFGDE with porous structures can serve as a good electron conductor and gas diffuser to load various catalysts for fine-tuning the products in CO_2RR. Overall, the design of microtubular flow-through GDEs for syngas production and the methodology to tune the syngas ratio still require further investigation.

To rationally design the novel HFGDEs for tuning syngas production, herein we develop a facile strategy to control the growth orientation of 2D zinc electrocatalysts on Cu-based HFGDEs. This is the first attempt to tune the product selectivity of HFGDEs by controlled growth of zinc nanosheets with controlled crystal facets towards production syngas with optimal CO/H_2 ratio. The pulse electrodeposition technique was applied for growing the zinc nanosheets, and the well-connected 2D zinc nanosheets on the surface of the electrode could potentially increase electrochemical active surface area (ECSA) and enhance the electron transfer. Furthermore, the ratio of the Zn (1 0 1)/Zn (0 0 2) facet can be controlled by adding surfactants, as they can change the surface free energy of the zinc crystal plane, leading to a preferential growth of a low surface free energy crystal facet. For syngas production, the ZncNS-HF with the largest ratio of Zn (1 0 1)/Zn (0 0 2) exhibited a higher current density and a higher syngas production compared with other Zn-coated HFGDEs. Moreover, conducting ZncNS-HF in non-GDE mode resulted in lower current densities, confirming the significant performance of HFGDEs for achieving high-rate and selective CO_2 reduction through maximizing triple-phase interfaces and local CO_2 concentration. This research provides guidance on designing novel HFGDE via facet-controlled growth electrocatalysts on HFGDE to tune syngas production.

2. Experimental method

2.1. Chemicals and materials.

Cu powder (99 % purity, 325 mesh) was purchased from Australian Metal Powders Supplies. Polyethersulfone (PES Ultrason E 6020P) was purchased from BASF, Germany. Zinc foil (99.9 %, 0.1 mm) was purchased from Yudingda Metal Company, China. N-methyl-2-pyrrolidone (NMP), Zinc sulfate heptahydrate ($ZnSO_4{\cdot}7H_2O$, 99 % purity), cetyl trimethyl ammonium bromide (CTAB, molecular biology grade), Potassium chloride (KCl, 99 % purity), nitric acid (HNO_3, 70 % purity) phosphoric acid (H_3PO_4, 85 % purity) were purchased from Sigma-Aldrich Australia. Nafion 117 membranes were purchased from Chemours company. Ultra-pure deionized water (18.2 MΩ•cm) used in all the experiments was obtained from the Milli-Q® Direct 8 system. Carbon dioxide (99.999 % purity), Argon (99.999 % purity), and 5 %H_2/Ar were purchased from BOC gas company, Australia.

2.2. Fabrication of Cu hollow fiber (Cu HF)

The Cu HFs were fabricated via dry-wet spinning and sintering process, as shown in Fig. S1. Typically, to get a homogenous polymeric dope, the Cu powder (65 wt%), PES (8.75 wt%), and NMP (26.25 wt%) were mixed in the ball mill jar for 48 h at 300 rpm. Then, the paste was vacuumed for 4 h at room temperature to remove the bubbles before slowly pouring it into a stainless-steel vessel. To start the extrusion process, the paste was pushed through a spinneret rig, and the bore fluid (DI water) as inner coagulant liquid was pumped through the bore of the spinneret. In the meantime, the phase inversion outside of the hollow fiber starts once the fiber comes down to the water bath. To remove the NMP entirely, the fibers must be kept in the bath overnight. After that, the fibers were dried at room temperature for 24 h. To fully reduce Cu hollow fiber with good strength, the green fibers were first calcinated in the air at 600 °C for 3 h to remove PES. After that, the copper oxide fibers were taken out and immersed into a 0.2 M $NaBH_4$ solution for 3 h. Lastly, the fibers were calcinated in 5 %H_2/Ar at 700 °C for 3 h to fully reduce and increase their strength. The fibers were stored in the N_2 atmosphere before further tests.

2.3. Zinc catalysts electrodeposition on Cu HF

The growth of zinc nanosheets on Cu hollow fiber was performed on a three-electrode system. Before the deposition, the counter electrode, a piece of zinc plate (2×6 cm^2, thickness 0.1 mm), was immersed into 1 M HNO_3 solution for 30 min to remove the oxide surface and then rinsed with ethanol and deionized water before drying at N_2. The Cu HFs were electropolished at 85 % phosphoric acid at 2 V for 120 s before electrodeposition. To prepare the zinc catalysts-based hollow fiber electrode, the Cu hollow fiber was first immersed into a 0.2 M $ZnSO_4$ solution as a working electrode, and an Ag/AgCl with 3 M NaCl solutions worked as a reference electrode. Then, applied −1.4 V (vs. Ag/AgCl) on potentiostat, on time 1 s, off time 3 s, set 250 cycles. A nitrogen flow rate was kept purging into the electrolytes during the electrodeposition process. The sample was synthesized via the above steps named zinc nanosheet hollow fiber (ZnNS-HF), and the zinc-controlled nanosheet hollow fiber (ZncNS-HF) was also prepared by the same procedure except adding 1 mM CTAB in 0.2 M $ZnSO_4$ electrolyte. In contrast, a comparison sample was prepared via a continuous electrodeposition method at −1.4 V (vs. Ag/AgCl) for 250 s in 0.2 M $ZnSO_4$ solution, named zinc micro particle hollow fiber (ZnMP-HF). Afterwards, the samples were raised with deionized water multiple times before drying with N_2.

2.4. Characterizations

The surface and cross-section morphology of HFGDEs were observed

by scanning electron microscopy (SEM, JOEL-7100F). The nanostructures of zinc nanosheets were inspected by high-resolution transmission electron microscopy (HRTEM, Hitachi HF 5000, Japan). The crystalline structures of the bulk phase HFGDEs were analyzed by X-ray diffraction (XRD, Bruker advanced X-ray diffractometer, Cu Kα (λ = 1.5405\AA) radiation source, Japan). X-ray photoelectron spectroscopy (XPS) was applied to analyze the surface valence state and surface compositions of the HFGDEs. XPS was conducted on a Kratos Axis ULTRA XPS with a monochromatic Al Kα radiation source (1486.6 eV) at 15 kV (10 mA) and a hemispherical electron energy analyzer (165 nm). CASA® software was used to analyze the XPS data, calibrated to the C 1 s signal at 284.4 eV as the reference. The morphology and thickness of zinc nanosheets were investigated on an atomic force microscope (Bruker MultiMode 8) at a Scanasyst-Air mode. The cantilever of the probe (Scanasyst-Air) used in all specimens has a spring constant of 0.4 N/m and a tip radius of 2 μm. A small amounts of zinc nanosheets were carefully exfoliated and dispersed into ethanol solutions. After ultrasonication for 1 h, a drop of this suspension mixture was cast on a silicon wafer, followed up with overnight drying before AFM analysis.

2.5. Electrochemical measurements

The electrochemical CO_2 electroreduction measurement were performed in a home-built H-cell using HFGDEs as working electrode. The working electrode was sticked into a ¼ copper tube via conductive silver epoxy, and the other ends as well joints were sealed and covered with non-conductive and gas-tight epoxy, with an exposed length of 2 cm. The geometric area of Cu HF is 0.817 cm^2 (S=πDoutL=π×1300×0.0001×2=0.817 cm^2, where S is the electrode area, Dout is the outer diameter of hollow fiber, and L is the length of hollow fiber For the HF hollow fiber). A Pt mesh (3×3 cm^2) was used as a counter electrode. An Ag/AgCl (3 M NaCl, BASi, USA) as reference electrode was put near the working electrode, the distance is between these two was around 1 cm. Nafion 117 Proton Exchange Membrane was used to separate the anode and cathode chambers. The potentials applied on the potentiostat (Autolab PGSTA302N with FRA32M) were converted the reversible hydrogen electrode (RHE) scale via E (V vs. RHE) = E (V vs. Ag/AgCl)+0.209+0.0591pH. The potential in this manuscript was used in RHE scale without RS competence. The pH value for 0.5 M KCl were measure by a pH meter (TPS, WP-Plus), and the value is around 3.8 in CO_2 saturated 0.5 M KCl solution. A 0.5 M KCl solution was used as both cathode and anode electrolyte. Before test, the H-Cell was vacuumed and kept purging with a 20 ml/min CO_2 for 30 min. The working electrode was reduced at −1 V for 30 min to remove the zinc oxide due to the spontaneous oxidization when the electrode exposed to the air.

The dual-layer capacitance (Cdl) of ZncNS-HF HFs was conducted to evaluate the electrochemically active surface area (ECSA) of the electrode at different scan rates starting from 20 to 100 mV/s via:

$$C_{dl} = J/\frac{dV}{dt} \tag{1}$$

Here, C_{dl} is the capacitance, the current density J is at the center of 0.1 V electrochemical window, and dV/dt is the cyclic voltammetry (CV) scan rate. The CV scans were carried out at 0.5 M CO_2 saturated KCl solution while purging CO_2 through the HFGDE samples.

Liner scanning voltammetry (LSV), with the sweeping rate of 5 mV/s, and from –0.65 V to −1.3 V (vs. RHE) were obtained in CO_2-saturated 0.5 M KCl after 30 min gas purging. The electrochemical impedance spectroscopy (EIS) test was conducted at a relatively lower potential of −1 V (vs. RHE) to evaluate the kinetics of charge transfer hollow fiber electrodes. Chrono amperometry (CA) was performed at potentials between −0.9 and −1.3 V (vs. RHE) to obtain the Faradaic efficiency (FE) of at different potentials. Gas and liquid samplings were done after 1000 s of applying potential and reaching the steady-state condition.

Gaseous products were analysed with a Shimadzu 2014 GC, equipped with a ShinCarbon packed column (ST 80/100, 2 mm ID, 1/8 OD Silico, Restek). H_2 was detected by a thermal conductivity detector (TCD) and the rest of the gases were detected on a flame ionization detector (FID). The FE of gaseous products were determined via the following equation:

$$FE_i = \frac{e_i \times F \times P \times V \times x_i}{J \times R \times T} \times 100\% \tag{2}$$

where, e_i is the electron transfer required to produce one mole of a gaseous product (2 for H_2 and CO), x_i is the concentration of the products in the reactor gas outlet flow measured by GC, V is the exit gas volumetric flow rate, measured by a digital flow meter, P is the atmospheric pressure (101.3 kPa), and J is the current (A) obtained from the potentiostat.

Liquid products was measured by a high-performance liquid chromatography (HPLC) (Shimadzu, Hi-Plex H, 7.7×300 mm, 8 μm column, SPD-20A/20AV UV–Vis detector). Only trace amounts ($FE_{formate} < 2$ %) of formate detected by HPLC at high overpotential.

The stability assessment was evaluated in a customized flow cell, employing peristaltic pumps to circulate electrolytes (0.5 M KCl) in the anodic and cathodic parts. Anode and cathode compartments had a volume of 54 ml, and two extra reservoir containers with a volume of 250 ml were used for catholyte and anolyte circulation. The circulation rate was set at 10 ml/min, with CO_2 purging maintained at 30 ml/min. Samplings of both liquid and gas were performed once every hour. The reported data for each electrochemical test is the average of three repeated measurements.

3. Results and discussion

3.1. Microstructure and morphology analysis

The growth of nanostructure catalysts on metal substrates via electrodeposition varies from multiple parameters such as substrate, composition and concentration of electrolyte, surfactants, deposition methods, applied potential/current, and duration time [40,43,44]. The electrodeposition strategy to tune the morphology of electrodeposited 2D Zn catalysts on Cu HF is shown in Fig. 1a. The pulse electrodeposition technique was applied to prepare the ZnNS-HF sample and the ZncNS-HF sample with the assistance of surfactant (Fig. 1a). The gas diffusion electrode was made via sealing one side of hollow fibers, and the CO_2 gas can diffuse through the porous walls of fibers, being reduced to CO at applied potentials. The cross-section SEM image (Fig. 1b) revealed a hierarchically porous Cu HF with a uniform wall thickness of 140 μm and a diameter of 1.3 mm. The Cu HF with good metal strength can serve as a good electron conductor due to its low ohmic resistance and a porous gas diffuser to reduce CO_2 mass transportation, facilitating the CO_2/electrolyte/catalyst interface formation, and enabling stable electrochemical experiments [40,42]. After the Zn deposition on Cu HF, the ZnNS-HF and the ZncNS-HF both turned to silver-grey color, indicating the formation of zinc layer on the Cu HF surface (Fig. 1c). The zinc catalyst layer thickness is around 14 μm, 12 μm, and 13 μm for ZncNS-HF (Fig. S2a), ZnNS-HF (Fig. S2b), and ZnMP-HF (Fig. S2c), respectively. The thick zinc layer could primarily prevent the CO_2RR active copper sites underneath from contributing to the reaction as the CO_2RR mainly occurs on the outside surface of the electrode in a gas-penetrating mode GDE. The fairly similar thickness of the zinc layer for the three samples is due to the identical applied potential, duration time of on-potential, and electrolyte concentration during the electrodeposition step. The hollow fiber geometry parameters, including gas permeability, were summarized in Table S1. We could see with the electrodeposition of different zinc nano catalysts on copper hollow fiber, the pressure drops increased, and the gas permeability slightly decreased. This means that the zinc coverage did not lead to blockage of HFGDE pores and could retain the

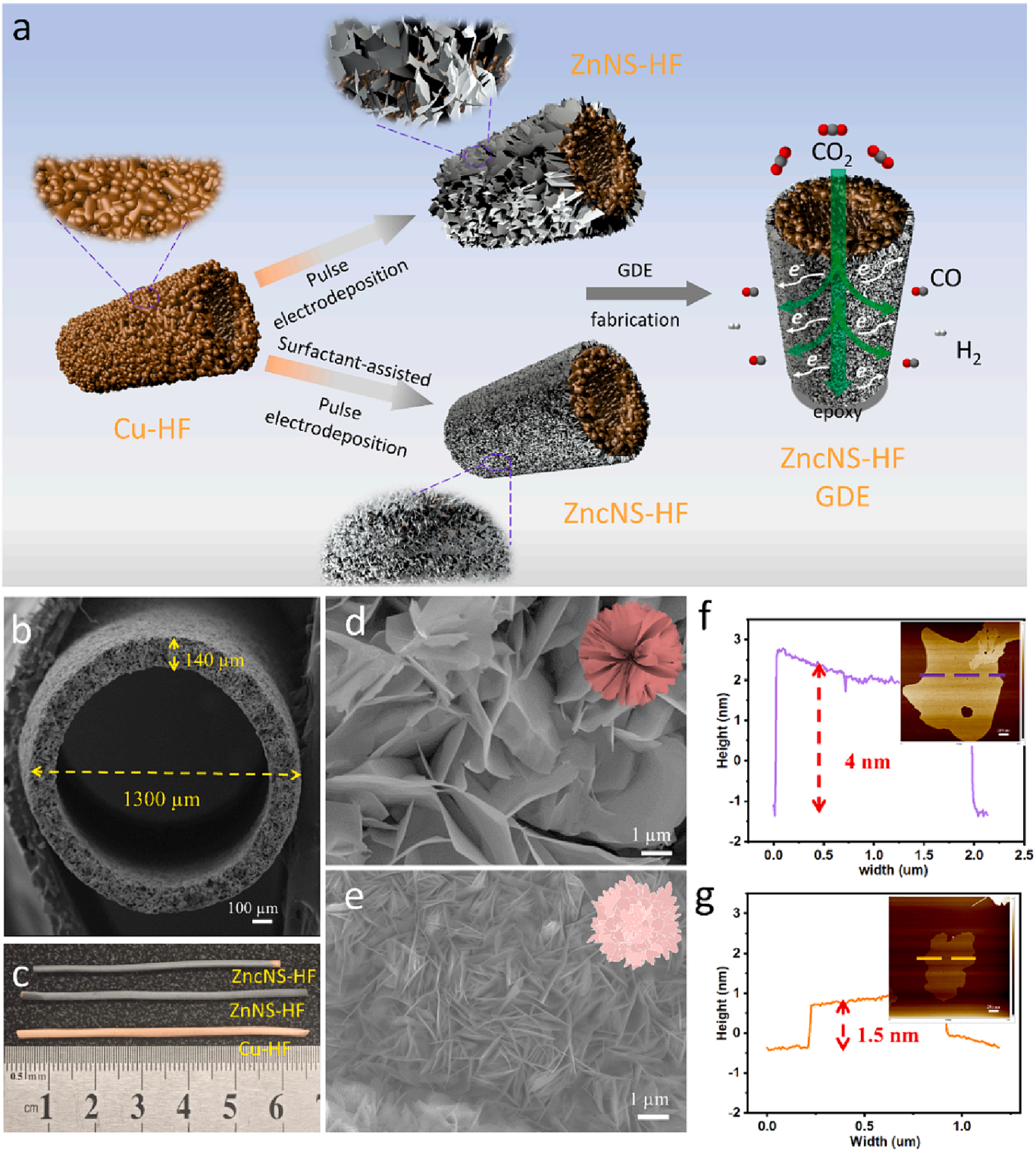

Fig. 1. (a) Schematic illustration of preparing Zn catalysts-based HFGDEs via pulse electrodeposition; (b) cross-section SEM image of ZncNS-HF; (c) optical photo images of Cu HF, ZnNS-HF, and ZncNS-HF; SEM images of ZnNS-HF (d), and ZncNS-HF (e); height profiles and AFM images (insertion) of ZnNS-HF (f), and ZncNS-HF (g) via AFM step analysis.

good gas delivery property of hollow fiber to provide sufficient CO_2 for the reaction sites.

Pulse electrodeposition has been practiced as an effective technique for the growth of nanosheets or nanoplate catalysts due to the multiple "on" and "off" potential cycles [38,40]. In contrast, it is more likely to form the bulk phase particles via continuous electrodeposition [45]. The ZnMP-HF was prepared by continuous electrodeposition at −1.4 V vs. Ag/AgCl for a period of 250 s. The zinc sheets were aligned and stacked to form bulk-phase zinc with a large particle size over 5 μm (Fig. S2d). That is because the zinc ions have been continuously consumed, leading to a concentration polarization near the Cu HF surface, forming different sizes of zinc particles based on local zinc ions concentration. Compared

to continuous electrodeposition, pulse electrodeposition can replenish zinc ions to the diffusion layer and lower the concentration gradient from the bulk electrolyte to the cathode surface [40,43]. The cell-off duration during the pulse electrodeposition process could allow the zinc ions to diffuse uniformly near the electrode and supply the electrodeposition consumption. The concentration of zinc ions near the electrode plays a vital role in determining the nucleation rate and crystal growth rate during the cathodic electrodeposition process. A sufficient concentration of zinc ions can promote the uniform growth of nanosheet structures [44]. From Fig. 1d, we can see a large size of zinc nanosheets (above 2 μm) formed by the pulse electrodeposition method. The thickness of samples was also measured by AFM step analysis (Fig. 1f), and it was around 3–5 nm for zinc nanosheets.

The adsorption of surfactants on the electrodes could adjust the kinetics of the electron transfer, tailor the growth of metal crystals, and further tune the morphology of electrodeposited catalysts [45]. Herein, 0.1 mM, 0.5 mM, and 1 mM cationic surfactant CTAB (Cetyltrimethylammonium bromide) was introduced in the 0.2 M $ZnSO_4$ electrolyte to further tune the growth of zinc nanosheets and morphology for enlarging the active surface area. After applying the negative potential, the cationic CTAB molecular will approach the surface of Cu HF, resulting in blocking some active sites for the deposition of zinc ions. From Fig. S3, when the same potential of −1.4 V (vs. Ag/AgCl) was applied during the electrodeposition process, the resulting current density was reduced with increasing the concentration of CTAB. This result is usually explained by the partial coverage of the electrode surface via CTAB, which decreases the nucleation rate of zinc ions. The strong blocking effect could lead to an increase in the nucleation number

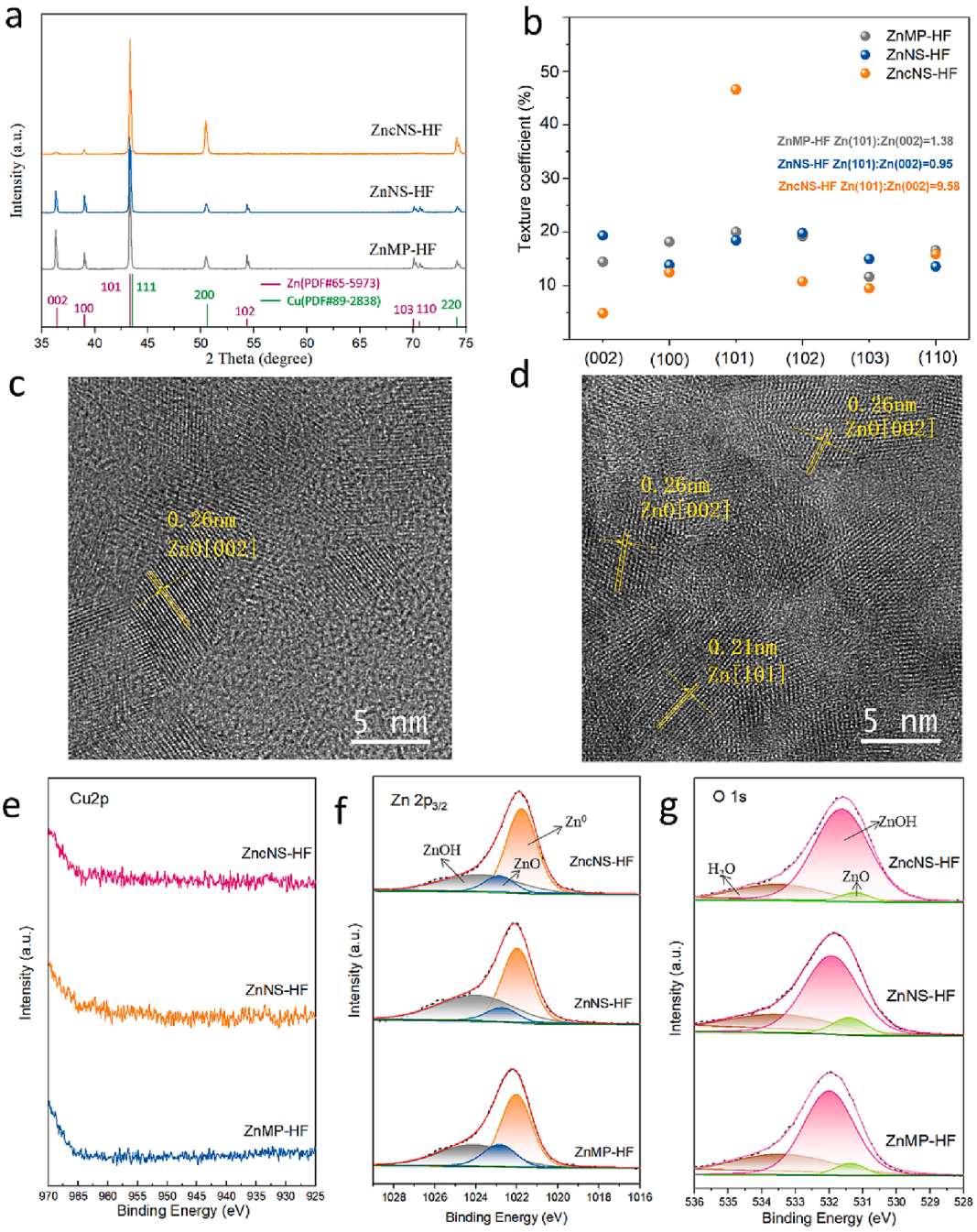

Fig. 2. (a) XRD patterns of Zn-deposited Cu HF; (b) Texture coefficient data of Zn-deposited Cu HF; HRTEM images of the ZnNS-HF sample (c), and ZncNS-HF sample (d); XPS spectra of Cu 2p (e), Zn $2p_{3/2}$ (f), and O 1 s (g) composition of Zn species on HFs.

and smaller grain size of zinc nanosheets [45,47]. From Fig. S4, we could observe the size of zinc nanosheets become smaller, and coverage density increased with the increasing concentration of CTAB in the electrolyte in the different magnifications of SEM images. A smaller size of zinc nanosheets (around 1 μm) was observed in the ZncNS-HF sample (Fig. 1e), and the thickness of nanosheets (around 1–2 nm) was also measured by AFM step analysis (Fig. 1g). The increased coverage density and the reduced thickness of deposited nanosheets could provide an enlarged electrochemical active surface area (ECSA) for the electrochemical reduction of CO_2.

X-ray diffraction (XRD) patterns of bulk phase ZnMP-HF, ZnNS-HF, and ZncNS-HF are shown in Fig. 2a. Three Copper metallic peaks at 43.3°, 50.4°, and 74.1° are detected in all samples, corresponding to Cu (1 1 1), (2 0 0), and (2 2 0) crystal planes of Cu (PDF#89–2848) [42]. The results are in accordance with the peaks observed in the origin Cu HF (Fig. S5a), and we can conclude that the copper crystal phase does not change after the electrodeposition of zinc ions on the Cu HF surface. The main zinc characteristic diffraction peaks at 36.3°, 39.0° and 43.2° corresponding to (0 0 2), (1 0 0), and (1 0 1) crystal planes of Zn (PDF#65-5973), which confirms the formation of metallic zinc layer during the electrodeposition process [38]. The ZnMP-HF sample has a relatively high intensity of the Zn (0 0 2) facet, and that is because the Zn (0 0 2) facet has the lowest surface free energy for zinc crystal growth, resulting in a dominant Zn (0 0 2) facet in the zinc bulk phase. A high-intensity Zn (0 0 2) facet is still detected in the ZnNS-HF sample due to the preferring growth in the low surface free energy Zn (0 0 2) facet although the morphology was tuned into nanosheet structures with applied pulse electrodeposition techniques [45,47]. In contrast, the ZncNS-HF sample has the lowest intensity of Zn (0 0 2), and relatively high intensity of Zn (1 0 1). The introduction of cationic CTAB during the electrodeposition process can change the metal surface energy to control the crystal facet orientation [36,45]. In this case, the adsorption of cationic CTAB molecular could increase the surface free energy of Zn (0 0 2), leading to preferential growth of the Zn (1 0 1) facet.

To get more information from the XRD data, we calculated the texture coefficient (Eq. S2) of each crystal facet of zinc phase for all samples (Fig. 2b and Fig. S6). The ZncNS-HF sample derived from 1 mM CTAB addition has the highest ratio of Zn (1 0 1)/Zn (0 0 2), and the ratio of Zn (1 0 1)/ Zn (0 0 2) increased with relatively high concentration of CTAB addition. This result confirms that the crystal facet orientation has been changed by adding cationic surfactant CTAB during the preparation while regulating the metal surface free energy by manipulating the nucleation and growth rate in the electrodeposition step [36,45,47]. The crystal structures of electrodeposited zinc nanosheets were further studied by high-resolution TEM (HRTEM), as shown in Fig. 2c and d. For ZnNS-HF and ZncNS-HF samples, the detected characteristic spacings of 0.26 nm are for ZnO (0 0 2) lattice planes, and the formation of ZnO is due to moisture and oxygen in the air [38,48]. The characteristic spacing of 0.21 nm is for Zn (1 0 1), which is only detected in the ZncNS-HF sample, and the results are in accordance with the XRD analysis, showing that the Zn (1 0 1) is dominate facet in the bulk zinc phase.

To further investigate the electronic states of zinc catalysts on Cu HFGDE, we conducted the analysis with the high-resolution XPS, the XPS spectra of Cu 2p, Zn 2p, and O 1 s are shown in Fig. 2e–g, respectively. The detected Cu 2p peak at around 932.5 eV in Cu HF (Fig. S5b) completely disappeared in all three samples (Fig. 2e), indicating a uniform zinc catalyst layer covering the Cu HF outside surface [36]. Considering the high coverage density and uniformity exhibited in the low-magnification SEM images (Fig. S4) and the thickness of catalyst layers of zinc-coating HFs is more than 10 μm (Fig. S2), and in a CO_2 penetrating mode, the CO_2RR mainly occurs on the outside surface of the electrode, so a thick and uniform zinc layer could primarily contribute to the reaction. The Zn $2p_{3/2}$ can be deconvoluted into three peaks (Fig. 2f), and the lowest binding energy peak at around 1021.7 eV is associated with the metallic Zn (Zn^0 state). In contrast, the highest binding energy peak (1023.8 eV) is linked to the Zn-OH bonding, and the other one is Zn-O bonding (1022.8 eV). The Zn $2p_{3/2}$ spectra of the ZncNS-HF, the ZnNS-HF, and the ZnMP-HF samples are shifted slightly toward higher binding energies, 1021.7, 1021.9, and 1022.0 eV, respectively. The shifts of the XPS Zn $2p_{3/2}$ to higher binding energies are due to the increase of the Zn-O species on the surface [46,48]. To gain more insight, the proportion of different zinc states for all three samples was calculated in Table S2. The ZncNS-HF has the highest ratio of metallic Zn^0 state than that of the other two samples, in accordance with the lower binding energy at 1021.7 eV detected in this sample.

The deconvoluted signals for XPS O 1 s spectra of the ZncNS-HF sample consisted of three different peaks at 531.2, 532.0, and 533.4 eV (Fig. 2g). The binding energy peak at 531.2 eV is associated with the Zn-O species, while another peak at 532.0 eV, usually corresponds to the Zn-OH species. The binding energy peak at 533.4 eV can be attributed to the adsorbed water on the electrode surface. The moisture and the oxidation zinc species detected via XPS analysis are attributed to the oxidized metallic zinc after exposure to the air during the ex-situ XPS test. Combined with the XRD and XPS results, it can be confirmed that the zinc state in the ZncNS-HF sample is mainly in the metallic Zn^0 state, and it has a large ratio of the Zn (1 0 1)/Zn (0 0 2).

3.2. *Electrocatalytic CO_2RR performance*

The zinc catalyst-based HFGDEs were tested for CO_2RR to determine their efficiency for CO_2 conversion. Before each test, the sample was electro-reduced at −1.0 V vs. RHE for 30 min to remove the zinc oxide layer due to the spontaneous oxidization of metallic zinc after exposure to the air [48]. The electrocatalytic activity of zinc catalyst-based HFGDEs was evaluated by liner scanning voltammetry (LSV) at a 5 mV/s scan rate, shown in Fig. 3a. The ZncNS-HF showed a higher current density compared to the ZnMP-HF and the ZnNS-HF at a wide potential range from −0.9 to −1.3 V (vs. RHE). Additionally, the current density for all three samples increased when higher negative potentials were applied. The current density for ZncNS-HF reached 73.3 mA/cm^2 at −1.3 V (vs. RHE). The high current density for the ZncNS-HF sample is attributed to the increased electrochemical surface area (ECSA), and the well-connected nanosheet structure provides more active sites for CO_2RR. The dual-layer capacitance (Cdl) of the zinc catalyst-based HFGDEs was calculated from the CV cycles at different scan rates, presented in Fig. 3b. The result showed that the ZncNS-HF sample possessed a higher Cdl value (8.83 mF/cm^2) compared to the other two samples. This confirmed that the larger ECSA active sites lead to a higher current density regarding the ZncNS-HF sample. In addition, the electrochemical impedance spectroscopy (EIS) test was conducted at a relatively lower potential of −1 V (vs. RHE) to evaluate the kinetics of charge transfer for all three samples (Fig. 3c). The results showed a similar spectrum for zinc catalyst-based HFGDEs but with different impedance arc sizes. The distances between low-frequency and high-frequency intercepts of EIS spectra on the real axis represent the charge-transfer resistance of the reduction reactions at the given potential. The ZnMP-HF and ZnNS-HF showed a similar resistance, and the ZncNS-HF samples exhibited a smaller arc size, indicating a lower charge-transfer resistance. The existence of well-connected nanosheet structure promotes electron conductivity, increases the charge density, and decreases charge-transfer resistance, resulting in a faster rate of electron transfer on the ZncNS-HF sample. The improved charge transfer improves the CO_2RR reaction rate, in accordance with the high current density observed in LSV results.

To compare the CO_2RR performance on the different zinc catalyst-based HFGDEs, CO_2RR tests were carried out at a potential range from −0.9 to −1.3 V (vs. RHE) in CO_2 saturated 0.5 M KCl electrolyte. The main products are H_2, CO and formate for the original Cu HF(Fig. S8). The selectivity for both H_2 and formate reduced with applied more negative potential, while the selectivity for CO increased. Syngas is the main product of zinc catalysts coating samples, and the Faradaic efficiency (FE) of syngas for all three samples is above 90 % in the applied

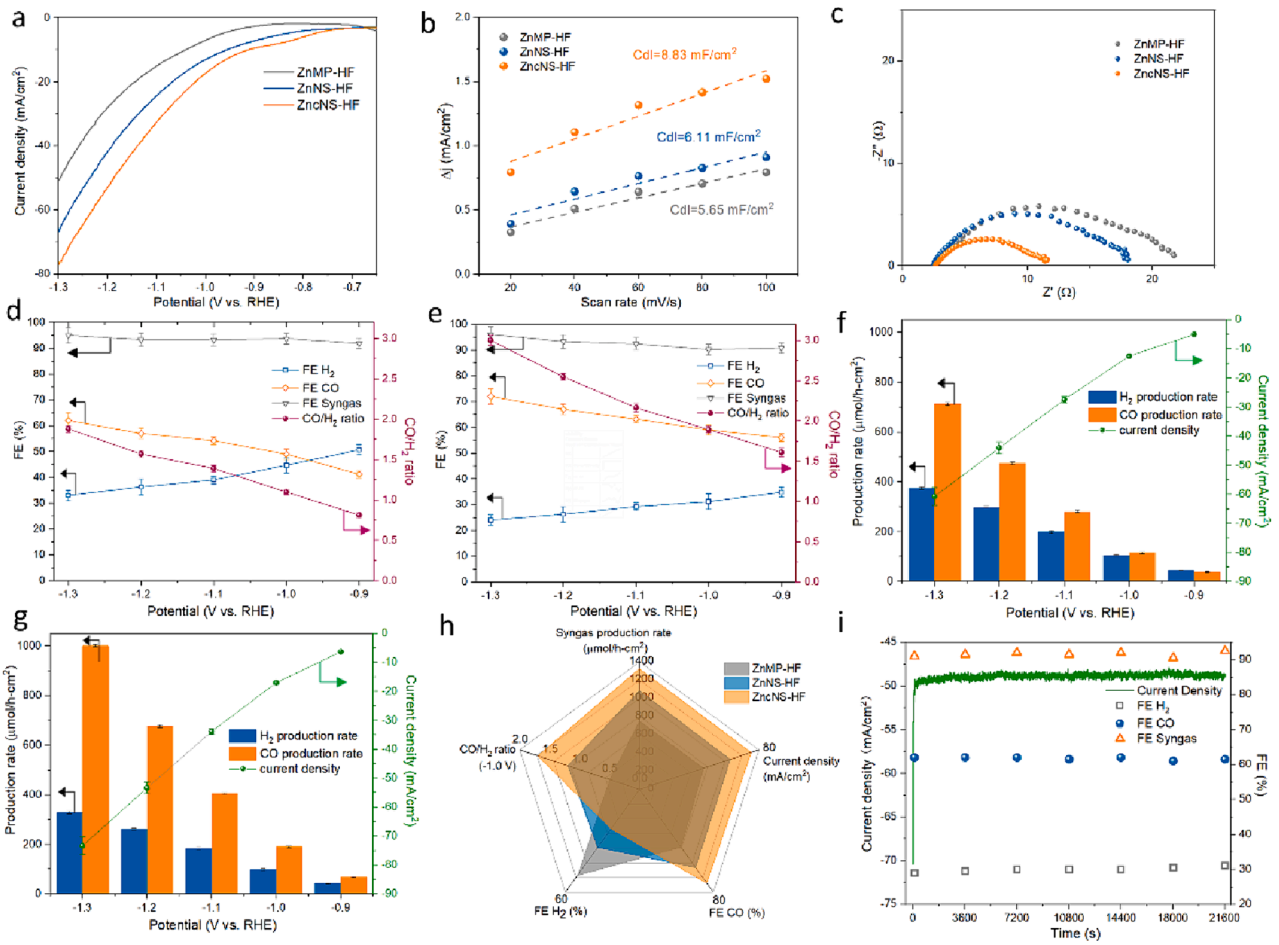

Fig. 3. (a) Linear sweep voltammetry (LSV) of ZnMP-HF, ZnNS-HF, and ZncNS-HF with CO_2 purging through; (b) Dual-layer capacitance (Cdl) of ZnMP-HF, ZnNS-HF, and ZncNS-HF electrodes; (c) Nyquist plots to evaluate electron resistance behavior of HFGDEs; Faradaic efficiency of syngas, CO and H_2, and CO/H_2 ratio for ZnNS-HF electrode (d), and ZncNS-HF electrode (e); CO and H_2 production rate and current density for ZnNS-HF electrode (f), and ZncNS-HF electrode (g); (h) Overall performance comparison for HFGDEs; (i) long-term operation of ZncNS-HF sample in flow-cell for CO_2RR in 0.5 M KCl.

potential (Fig. 3d, e, and Fig. S7a). Only a small amount of formic acid with a Faradaic efficiency of less than 2 % is detected by the HPLC. The ZnMP-HF sample showed the highest CO/H_2 ratio of 0.9 for the ZnMP-HF sample at −1.3 V (vs. RHE), with the FE for CO of 44 % and the FE for H_2 of 52 % (Fig. S7a). The CO/H_2 ratio on ZnNS-HF reached the maximum value of 1.6 with 62 % of FE for CO and 34 % of FE for H_2 at −1.3 V (vs. RHE) presented in Fig. 3d. As shown in Fig. 3e, ZncNS-HF revealed the highest CO/H_2 ratio of 3.0 at −1.3 V (vs. RHE) with a highest FE for CO of 72 % and lowest FE for H_2 of 24 %.

In a gas penetrating mode, HFGDEs CO_2RR occurs on the outer layer catalyst of the electrode because CO_2 is pushed through the electrode via a pressure difference, and the inner pores are not flooded by the electrolyte. The HER of ZnNS-HF and ZncNS-HF has been suppressed by coating the zinc nanosheet layer compared with the Cu HF with a high HER at applied potentials. The cross-section SEM images (Fig. S2) have shown the zinc catalyst layer of these samples is more than 10 μm. The Cu-Zn interactions will become extremely weak when the Cu substrate is fully covered with zinc nanosheets so the contribution from copper substrate is negligible. The high-coverage density and well-connected zinc nanosheet structure in the ZncNS-HF sample provide an enlarged electrochemical active surface area (ECSA) and decreased charge-transfer resistance, which resulted in a higher current density (Fig. 3a). The XRD results have shown these catalysts exhibited different ratios of Zn (1 0 1)/Zn (0 0 2), and from the previous reports [36–38], the Zn (1 0 1) facet has more CO_2RR activity for CO production, and the Zn (0 0 2) facet prefers to produce H_2. Therefore, the different FE for CO of these three samples is mainly attributed to the different crystal facet ratios in the zinc bulk phases. The ZncNS-HF has the largest ratio of Zn (1 0 1) to Zn (0 0 2) compared to that of the other two samples, leading to the highest FE for CO.

For the electrochemical reduction of CO_2 to CO, three reaction steps were widely acknowledged as in following Eqs. (3)–(5),

$$CO_2(aq) + [H^+ + e^-] \rightarrow COOH^*(aq) \quad (3)$$

$$COOH^*(aq) + [H^+ + e^-] \rightarrow CO^*(aq) + H_2O(aq) \quad (4)$$

$$CO^*(aq) \rightarrow CO(g) \quad (5)$$

where * represents a catalytically active site. At the beginning of the reaction, CO_2 is adsorbed on the surface of the electrode and reduced to CO_2* via one electron from the electrochemical process and then to the intermediate COOH* via a proton transfer step. Lastly, most of the COOH* intermediate is reduced with a proton and an electron to CO* that desorbs from Zn to produce the main product CO. A highly selective zinc catalyst for the electrochemical conversion of CO_2 to CO is required to have a strong binding ability to COOH* and weak adsorption to CO*. In the meantime, the zinc catalyst should also have a low binding affinity for H* to suppress the competitive HER. Previous studies have proved that the formation of COOH* was associated with an uphill process, so it is the reaction-rating determining step [36–38]. The Zn (1 0 1) exhibited a stronger COOH* binding affinity than that of Zn (0 0 2), while the Zn (0 0 2) facet requires a low energy barrier to produce H_2 compared to Zn

(1 0 1) [37,38]. Thus, the CO/H_2 product ratio can be controlled by tailoring the crystal facet ratio of the Zn electrode.

The production rate is also an important factor to consider in meeting the requirement of industry application of syngas. The syngas production rate (CO + H_2 production rate) for all three samples (Fig. 3f, g, and Fig. S7b) increased with the application of larger negative potentials, which aligns with the current density trend. In Fig. 3g, the ZncNS-HF can produce a 1328.6 μmol/h•cm^2 syngas production rate at −1.3 V (vs. RHE), 1086.9 μmol/h•cm^2 and 754.0 μmol/h•cm^2 for ZnNS-HF (Fig. 3f) and ZnMP-HF (Fig. S7b), respectively. The overall performance comparison for the zinc catalyst-based HFGDEs was presented in Fig. 3h. The ZncNS-HF sample demonstrates outstanding performance in terms of syngas production rate, current density, and FE for CO compared to the other two samples. At a specific potential at −1.0 V (vs. RHE), the ZnMP-HF with a CO/H_2 ratio around 0.5 is suitable for methanol synthesis; the ZnNS-HF with a CO/H_2 ratio around 1.1 could suit syngas fermentation; the ZncNS-HF with a CO/H_2 ratio around 1.7 can target Fischer-Tropsch synthesis.

The stability of the electrocatalyst is another crucial factor considered for commercial application. The long-term stability of the ZncNS-HF for CO_2RR performance was conducted in a customized flow cell (Fig. S9). To run the flow cell, the CO_2 flow rate was kept at 30 ml/min, and the electrolytes (0.5 M KCl) were circulated at 10 ml/min in both anode and cathode chambers. The ZncNS-HF exhibited a stable performance for current density and FE of syngas over a period of 6 h at −1.1 V (vs. RHE), shown in Fig. 3i. In addition, a higher current density of 48 mA/cm^2 was obtained compared with the 36 mA/cm^2 from the H-cell (Fig. 3g), which is attributed to the stabilized pH in the electrolyte and sufficient CO_2 availability near the electrode. The syngas Faradaic efficiency was above 90 % during the whole test, and the FE for CO was around 62 % with no noticeable decrease, which shows favourable stability for the ZncNS-HF electrode. Moreover, the SEM image (Fig. S10a) of the electrode surface for the sample after the long-term reaction showed intact nanosheet morphology; therefore, the electrocatalyst on the fabricated electrodes can maintain their morphology at a relatively long operation. XRD pattern (Fig. S10b) of the ZncNS-HF after the reaction also demonstrated the Zn (1 0 1) as the dominant phase, the texture coefficient of Zn (1 0 1)/Zn(0 0 2) = 9.78, similar to the value before the reaction. The crystal facet ratio of the ZncNS-HF is the key to keeping the stable CO/H_2 ratio during the long-term operation. The performance of the zinc catalyst-based HFGDEs in this study is compared with the recent state-of-the-art studies to produce syngas as the main product from CO_2RR in Table S3. The zinc catalyst-based HFGDEs exhibited outstanding performance for current density and total Faradaic efficiency for syngas compared with other conventional planar GDEs, indicating the high potential of rational design HFGDEs for electrocatalytic CO_2 conversion to syngas.

3.3. The mechanism of CO_2 delivery in HFGDEs

The gas delivery configuration of zinc catalyst-based HFGDEs is flow-through or gas penetration, meaning a pressure building up in the lumen side of the tube pushes the gas penetrating through the hollow fiber wall to the electrolyte side. This differs from planar electrodes, where gas diffuses to the catalyst layer of electrode, forming a gas concentration gradient from bulk electrolytes to the cathode [22]. In the GDEs with

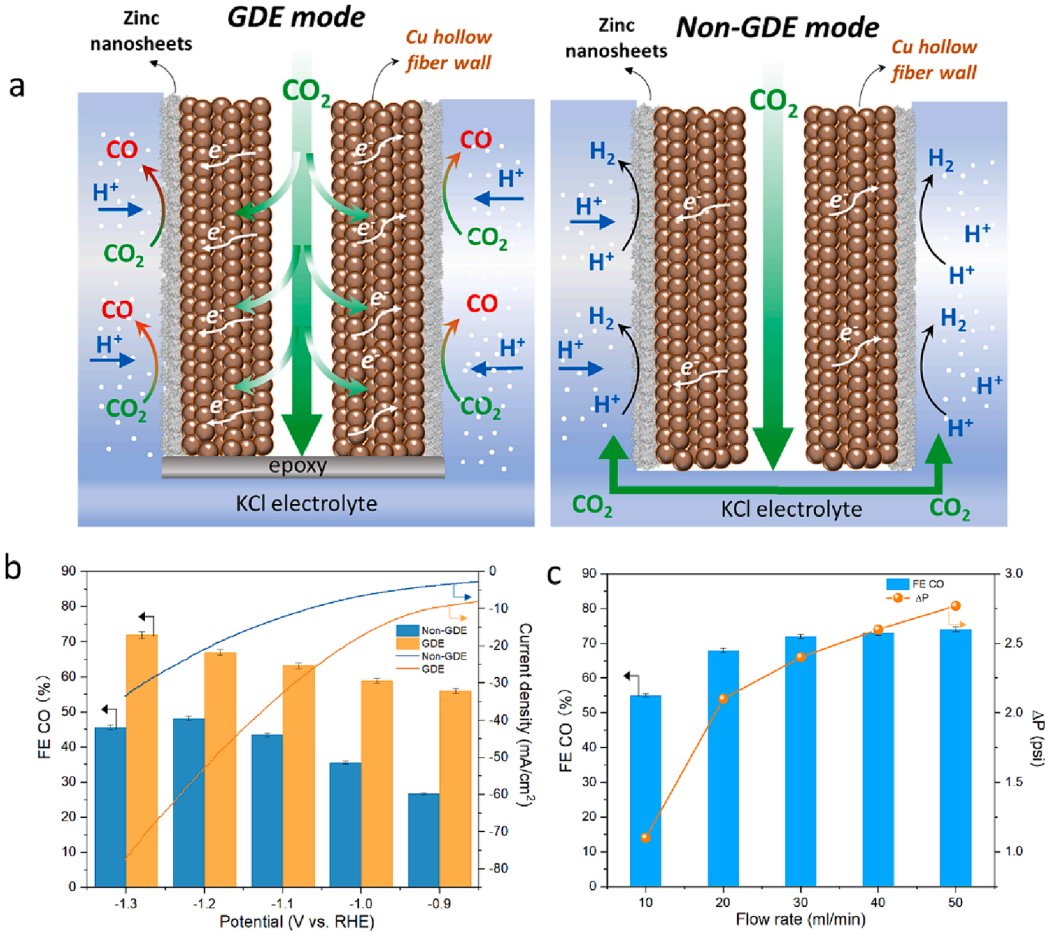

Fig. 4. (a) Schematic of CO_2 delivery mechanism in GDE and non-GDE mode; (b) Faradaic efficiency of CO and current density for ZncNS-HF sample in GDE and non-GDE mode; (c) Faradaic efficiency of CO and pressure drop at a different CO_2 flow rate for ZncNS-HF sample.

flow-through mode, the gas concentration gradient is diminished due to pushing the gas into the electrolyte, therefore providing an enriched CO_2 supply. The CO_2 concentration near the electrode is critical for CO_2 reduction, particularly under high current densities, the rapid energy supply causes a significant CO_2 consumption. If the CO_2 concentration is low, it will lead to a high rate of hydron evolution due to the abundant protons in the electrolytes [24,28]. To further investigate the CO_2RR mechanism in the ZncNS-HF sample, we also tested the ZncNS-HF in non-GDE mode, which is made by leaving one side of the hollow fiber open, as shown in Fig. 4a. The CO_2 is mainly delivered through that end open side and dissolve into the electrolyte for the reaction. The same electrode in GDE and non-GDE modes shows obvious difference in electrochemical activity, the ZncNS-HF in GDE modes shows a higher current density and high FE for CO (Fig. 4b). That is because the CO_2 is penetrated through the porous hollow fiber wall, which can provide a sufficient supplement of CO_2, leading to improved triple-phase interface formation and optimized kinetics for CO_2RR. The CO_2RR dominates in GDE-mode, while this contrasts in non-GDE mode due to insufficient CO_2 supply and abundant protons from the electrolyte.

To further investigate the CO_2RR performance on the ZncNS-HF sample, we tested its performance with a different flow rate from 10 ml/min to 50 ml/min. A sharp pressure drop is observed when the flow rate increases from 10 to 20 ml/min (Fig. 4c), leading to an increase in current density (Fig. S11) and Faradaic efficiency for CO (Fig. 4c). That is because, in the porous hollow fiber GDE configuration, a small pressure will build up with CO_2 gas feeding to overcome the capillary pressure, and CO_2 gas will first penetrate those pores with relatively larger pore sizes. The increased flow rate with larger pressure built-up inside the fiber could lead to improved CO_2 gas distribution on the external surface of ZncNS-HF, leading to the creation of more triple phase interfaces to boost their CO_2RR performance [49]. In addition, the relatively low current density and FE for CO at 10 ml/min indicate that the reaction is deprived of sufficient CO_2 supply to the reaction zone. The increased Faradaic efficiency for CO is also due to a large ratio of Zn (1 0 1) facets in the bulk phase of ZncNS-HF. With increasing the flow rate from 30 to 50 ml/min, the current density and FE CO only increase very slightly, which indicates that the availability of CO_2 gas on the ZncNS-HF electrode is relatively saturated. The energy efficiency will drop with further increased flow rate [26,50]. Herein, we conclude that the rational design of electrodes with the combination of the HFGDE configuration and the catalyst facet orientation design has a high potential for syngas production with a high current density and production rate. Future studies should aim to improve the electron transfer and gas distribution properties of HFGDEs, as well as loading more active/selective catalysts for other desired products.

4. Conclusion

In this study, the metallic microtubular GDEs were fabricated with controlled growth of facet-orientated zinc nanosheet catalysts for electrochemical conversion of CO_2 to syngas. It was found that the introduction of cationic surfactant CTAB could not only manipulate the nucleation of zinc ions around the GDE during the electrodeposition process but also can adjust the surface free energy to control the zinc crystal growth orientation. The porous metallic HFGDE can serve as a good electron conductor and gas diffuser, while the facet-orientated zinc nanosheets could tune the syngas ratio towards desired reactions. The ZncNS-HF sample with a large ratio of Zn (1 0 1)/Zn (0 0 2) exhibited a high current density of 73.3 mA/cm^2 and a high syngas production rate of 1328.6 μmol/h•cm^2 at applied potential −1.3 V (vs. RHE). The syngas Faradaic efficiency is greater than 90 % at a wide potential range of −0.9 to −1.3 V (vs. RHE), the ZnMP-HF with a tuneable syngas ratio from 0.4 to 0.9; ZnNS-HF with 0.8–1.9; and ZncNS-HF with 1.5–3, targeting different products. Moreover, the ZncNS-HF electrode was tested in both GDE and non-GDE modes, and it showed a high current density and Faradaic efficiency for CO in GDE mode. That is due to the sufficient CO_2 penetrating through the hollow fiber walls and reaching the catalyst/electrolytes interface in GDE mode. In contrast, most of CO_2 can only dissolve into the electrolyte, forming a CO_2 concentration gradient and leading to a long CO_2 diffusion path from the bulk electrolyte to the working electrode surface in non-GDE mode. Additionally, the pressure building up in the hollow fiber GDE could allow CO_2 gas to distribute on the electrode surface, creating more triple-phase reaction interfaces and facilitating the electrochemical reduction of CO_2. This study showcased the potential to engineer a stable structured electrode for syngas production by configuring a hollow fiber electrode and designing crystal facet-controlled electrocatalysts.

CRediT authorship contribution statement

Guoliang Chen: Writing – original draft, Writing – review & editing, Writing – original draft, Validation, Investigation, Formal analysis, Data curation. **Lei Ge:** Writing – review & editing, Writing – original draft, Supervision, Resources, Project administration, Methodology, Funding acquisition, Conceptualization. **Yizhu Kuang:** Writing – review & editing, Investigation, Data curation. **Hesamoddin Rabiee:** Writing – review & editing, Validation, Methodology, Investigation, Funding acquisition, Formal analysis. **Beibei Ma:** Formal analysis, Data curation. **Fatereh Dorosti:** Formal analysis, Data curation. **Ashok Kumar Nanjundan:** Writing – review & editing, Formal analysis. **Zhonghua Zhu:** Writing – review & editing, Resources, Project administration. **Hao Wang:** Writing – review & editing, Validation, Supervision, Resources, Project administration, Methodology, Funding acquisition.

Declaration of competing interest

The authors declare that they have no known competing financial interests or personal relationships that could have appeared to influence the work reported in this paper.

Data availability

Data will be made available on request.

Acknowledgements

We acknowledge financial support from the ARC Future Fellowship (FT220100166), Discovery project (DP190101782) and Centre of Excellence for Green Electrochemical Transformation of Carbon Dioxide (CE230100017). We acknowledge the UniSQ 2022 Capacity Building Grant awarded to Dr Hesamoddin Rabiee.

Appendix A. Supplementary data

Supplementary data to this article can be found online at https://doi.org/10.1016/j.cej.2024.151651.

References

[1] C.-T. Dinh, T. Burdyny, M.G. Kibria, A. Seifitokaldani, C.M. Gabardo, F.P. García de Arquer, A. Kiani, J.P. Edwards, P. De Luna, O.S. Bushuyev, CO_2 electroreduction to ethylene via hydroxide-mediated copper catalysis at an abrupt interface, Science 360 (2018) 783–787, https://doi.org/10.1126/science.aas9100.

[2] F.P. García de Arquer, C.-T. Dinh, A. Ozden, J. Wicks, C. McCallum, A.R. Kirmani, D.-H. Nam, C. Gabardo, A. Seifitokaldani, X. Wang, CO_2 electrolysis to multicarbon products at activities greater than 1 A cm^{-2}, Science 367 (2020) 661–666, https://doi.org/10.1126/science.aay4217.

[3] J.E. Huang, F. Li, A. Ozden, A. Sedighian Rasouli, F.P. García de Arquer, S. Liu, S. Zhang, M. Luo, X. Wang, Y. Lum, CO_2 electrolysis to multicarbon products in strong acid, Science 372 (2021) 1074–1078, https://doi.org/10.1126/science.abg6582.

[4] X. Wang, Z. Wang, F.P. García de Arquer, C.-T. Dinh, A. Ozden, Y.C. Li, D.-H. Nam, J. Li, Y.-S. Liu, J. Wicks, Efficient electrically powered CO_2-to-ethanol via suppression of deoxygenation, Nat. Energy 5 (2020) 478–486, https://doi.org/10.1038/s41560-020-0607-8.

[5] Z. Liu, X. Lv, S. Kong, M. Liu, K. Liu, J. Zhang, B. Wu, Q. Zhang, Y. Tang, L. Qian, Interfacial Water Tuning by Intermolecular Spacing for Stable CO2 Electroreduction to C2+ Products, Angew. Chem. Int. Ed. Engl. 62 (2023) e202309319.

[6] S. Han, W. Xia, S. Jia, J. Jiao, T. Yao, X. Dong, M. Wang, J. Zhai, J. Yang, Y. Xie, Boosting promote C_2 products formation in electrochemical CO_2 reduction reaction via phosphorus-enhanced proton feeding, Chem. Eng. J. 479 (2024) 147735, https://doi.org/10.1016/j.cej.2023.147735.

[7] X. Li, D. Kang, Z. He, J. Chen, F. Wang, Z. Zhang, Regulation of catalytic reaction performance of CO_2 with ethane by metal cation substitution on CeO_2 support, Chem. Eng. J. 484 (2024) 149047, https://doi.org/10.1016/j.cej.2024.149047.

[8] Y. Kuang, H. Rabiee, L. Ge, T.E. Rufford, Z. Yuan, J. Bell, H. Wang, High-concentration electrosynthesis of formic acid/formate from CO2: reactor and electrode design strategies, Energy Environ. Mat. 6 (2023) e12596.

[9] H. Rabiee, P. Yan, H. Wang, Z. Zhu, L. Ge, Electrochemical CO_2 reduction integrated with membrane/adsorption-based CO_2 capture in gas-diffusion electrodes and electrolytes, EcoEnergy 2 (2024) 3–21, https://doi.org/10.1002/ece2.23.

[10] F. Jiao, J. Li, X. Pan, J. Xiao, H. Li, H. Ma, M. Wei, Y. Pan, Z. Zhou, M. Li, Selective conversion of syngas to light olefins, Science 351 (2016) 1065–1068, https://doi.org/10.1126/science.aaf1835.

[11] N. Meng, W. Zhou, Y. Yu, Y. Liu, B. Zhang, Superficial Hydroxyl and Amino Groups Synergistically Active Polymeric Carbon Nitride for CO_2 Electroreduction, ACS Catal. 9 (2019) 10983–10989, https://doi.org/10.1021/acscatal.9b03895.

[12] C. Kong, G. Jiang, Y. Sheng, Y. Liu, F. Gao, F. Liu, X. Duan, Progress on Cu-based metal-organic frameworks for high-efficiency electrochemical CO_2 conversion, Chem. Eng. J. 460 (2023) 141803, https://doi.org/10.1016/j.cej.2023.141803.

[13] S. Cao, H. Chen, Y. Hu, J. Li, C. Yang, Z. Chen, S. Wei, S. Liu, Z. Wang, D. Sun, MXene-based single atom catalysts for efficient CO_2RR towards CO: A novel strategy for high-throughput catalyst design and screening, Chem. Eng. J. 461 (2023) 141936, https://doi.org/10.1016/j.cej.2023.141936.

[14] D. Wu, F. Jiao, Q. Lu, Progress and Understanding of CO_2/CO Electroreduction in Flow Electrolyzers, ACS Catal. 12 (2022) 12993–13020, https://doi.org/10.1021/acscatal.2c03348.

[15] J. Choi, J. Kim, P. Wagner, S. Gambhir, R. Jalili, S. Byun, S. Sayyar, Y.M. Lee, D. R. MacFarlane, G.G. Wallace, Energy efficient electrochemical reduction of CO_2 to CO using a three-dimensional porphyrin/graphene hydrogel, Energy Environ. Sci. 12 (2019) 747–755, https://doi.org/10.1039/C8EE03403F.

[16] M. Ma, K. Liu, J. Shen, R. Kas, W.A. Smith, In Situ fabrication and reactivation of highly selective and stable Ag catalysts for electrochemical CO_2 conversion, ACS Energy Lett. 3 (2018) 1301–1306, https://doi.org/10.1021/acsenergylett.8b00472.

[17] R. Shi, J. Guo, X. Zhang, G.I.N. Waterhouse, Z. Han, Y. Zhao, L. Shang, C. Zhou, L. Jiang, T. Zhang, Efficient wettability-controlled electroreduction of CO_2 to CO at Au/C interfaces, Nat. Commun. 11 (2020) 3028, https://doi.org/10.1038/s41467-020-16847-9.

[18] T. Li, E.W. Lees, M. Goldman, D.A. Salvatore, D.M. Weekes, C.P. Berlinguette, Electrolytic Conversion of Bicarbonate into CO in a Flow Cell, Joule 3 (2019) 1487–1497, https://doi.org/10.1016/j.joule.2019.05.021.

[19] Z. Xing, L. Hu, D.S. Ripatti, X. Hu, X. Feng, Enhancing carbon dioxide gas-diffusion electrolysis by creating a hydrophobic catalyst microenvironment, Nat. Commun. 12 (2021) 136, https://doi.org/10.1038/s41467-020-20397-5.

[20] M.P. Schellekens, S.J. Raaijman, M.T. Koper, P.J. Corbett, Temperature-dependent selectivity for CO electroreduction on copper-based gas-diffusion electrodes at high current densities, Chem. Eng. J. 483 (2024) 149105, https://doi.org/10.1016/j.cej.2024.149105.

[21] H. Rabiee, L. Ge, S. Hu, H. Wang, Z. Yuan, Microtubular electrodes: An emerging electrode configuration for electrocatalysis, bioelectrochemical and water treatment applications, Chem. Eng. J. 450 (2022) 138476, https://doi.org/10.1016/j.cej.2022.138476.

[22] H. Rabiee, L. Ge, X. Zhang, S. Hu, M. Li, Z. Yuan, Gas diffusion electrodes (GDEs) for electrochemical reduction of carbon dioxide, carbon monoxide, and dinitrogen to value-added products: a review, Energy Environ. Sci. 14 (2021) 1959–2008, https://doi.org/10.1039/D0EE03756G.

[23] R. Kas, K.K. Hummadi, R. Kortlever, P. de Wit, A. Milbrat, M.W. Luiten-Olieman, N. E. Benes, M.T. Koper, G. Mul, Three-dimensional porous hollow fibre copper electrodes for efficient and high-rate electrochemical carbon dioxide reduction, Nat. Commun. 7 (2016) 10748, https://doi.org/10.1038/ncomms10748.

[24] S. Li, X. Dong, J. Mao, W. Chen, A. Chen, G. Wu, C. Zhu, G. Li, Y. Wei, X. Liu, J. Wang, Y. Song, W. Wei, Highly Efficient CO_2 Reduction at Steady 2 A cm^{-2} by Surface Reconstruction of Silver Penetration Electrode, Small 19 (2023) e2301338.

[25] X. Dong, S. Li, C. Zhu, J. Mao, G. Wu, G. Li, G. Feng, A. Chen, Y. Wei, X. Liu, J. Wang, Y. Song, W. Chen, W. Wei, Highly efficient ampere-level CO_2 reduction to multicarbon products via stepwise hollow-fiber penetration electrodes, Appl. Catal. B 336 (2023) 122929, https://doi.org/10.1016/j.apcatb.2023.122929.

[26] S. Li, W. Chen, X. Dong, C. Zhu, A. Chen, Y. Song, G. Li, W. Wei, Y. Sun, Hierarchical micro/nanostructured silver hollow fiber boosts electroreduction of carbon dioxide, Nat. Commun. 13 (2022) 3080, https://doi.org/10.1038/s41467-022-30733-6.

[27] A. Chen, X. Dong, J. Mao, W. Chen, C. Zhu, S. Li, G. Wu, Y. Wei, X. Liu, G. Li, Y. Song, Z. Jiang, W. Wei, Y. Sun, Gas penetrating hollow fiber Bi with contractive bond enables industry-level CO_2 electroreduction, Appl. Catal. B 333 (2023) 122768, https://doi.org/10.1016/j.apcatb.2023.122768.

[28] C. Zhu, Y. Song, X. Dong, G. Li, A. Chen, W. Chen, G. Wu, S. Li, W. Wei, Y. Sun, Ampere-level CO_2 reduction to multicarbon products over a copper gas penetration electrode, Energy Environ. Sci. 15 (2022) 5391–5404, https://doi.org/10.1039/d2ee02121h.

[29] W. Wang, J. Duan, Y. Liu, T. Zhai, Structural Reconstruction of Catalysts in Electroreduction Reaction: Identifying, Understanding, and Manipulating, Adv. Mater. 34 (2022) e2110699.

[30] W. Shao, X. Zhang, Atomic-level engineering of two-dimensional electrocatalysts for CO_2 reduction, Nanoscale 13 (2021) 7081–7095, https://doi.org/10.1039/d1nr00649e.

[31] M.B. Ross, Y. Li, P. De Luna, D. Kim, E.H. Sargent, P. Yang, Electrocatalytic rate alignment enhances syngas generation, Joule 3 (2019) 257–264, https://doi.org/10.1016/j.joule.2018.09.013.

[32] M.B. Ross, C.T. Dinh, Y. Li, D. Kim, P. De Luna, E.H. Sargent, P. Yang, Tunable Cu enrichment enables designer syngas electrosynthesis from CO_2, J. Am. Chem. Soc. 139 (2017) 9359–9363, https://doi.org/10.1021/jacs.7b04892.

[33] H. Cheng, X. Wu, X. Li, X. Nie, S. Fan, M. Feng, Z. Fan, M. Tan, Y. Chen, G. He, Construction of atomically dispersed Cu-N_4 sites via engineered coordination environment for high-efficient CO_2 electroreduction, Chem. Eng. J. 407 (2021) 126842, https://doi.org/10.1016/j.cej.2020.126842.

[34] H. Yang, P. Zhang, X. Yi, C. Yan, D. Pang, L. Chen, S. Wang, C. Wang, B. Liu, G. Zhang, Constructing highly utilizable Fe-N_4 single-atom sites by one-step gradient pyrolysis for electroreduction of O_2 and CO_2, Chem. Eng. J. 440 (2022) 135749, https://doi.org/10.1016/j.cej.2022.135749.

[35] Q. He, D. Liu, J.H. Lee, Y. Liu, Z. Xie, S. Hwang, S. Kattel, L. Song, J.G. Chen, Electrochemical conversion of CO2 to syngas with controllable CO/H2 ratios over Co and Ni single-atom catalysts, Angew. Chem. Int. Ed. Engl. 59 (2020) 3033–3037, https://doi.org/10.1002/anie.201912719.

[36] B. Qin, Y. Li, H. Fu, H. Wang, S. Chen, Z. Liu, F. Peng, Electrochemical Reduction of CO_2 into Tunable Syngas Production by Regulating the Crystal Facets of Earth-Abundant Zn Catalyst, ACS Appl. Mater. Interfaces 10 (2018) 20530–20539, https://doi.org/10.1021/acsami.8b04809.

[37] J. Xiao, M.R. Gao, S. Liu, J.L. Luo, Hexagonal Zn Nanoplates Enclosed by Zn(100) and Zn(002) Facets for Highly Selective CO2 Electroreduction to CO, ACS Appl. Mater. Interfaces 12 (2020) 31431–31438, https://doi.org/10.1021/acsami.0c06891.

[38] H. Won da, H. Shin, J. Koh, J. Chung, H.S. Lee, H. Kim, S.I. Woo, Highly Efficient, Selective, and Stable CO_2 Electroreduction on a Hexagonal Zn Catalyst, Angew. Chem. Int. Ed. Engl. 55 (2016) 9297–9300, https://doi.org/10.1002/anie.201602888.

[39] H. Rabiee, L. Ge, J. Zhao, X. Zhang, M. Li, S. Hu, S. Smart, T.E. Rufford, Z. Zhu, H. Wang, Z. Yuan, Regulating the reaction zone of electrochemical CO_2 reduction on gas-diffusion electrodes by distinctive hydrophilic-hydrophobic catalyst layers, Appl. Catal. B 310 (2022) 121362, https://doi.org/10.1016/j.apcatb.2022.121362.

[40] H. Rabiee, L. Ge, X. Zhang, S. Hu, M. Li, S. Smart, Z. Zhu, Z. Yuan, Shape-tuned electrodeposition of bismuth-based nanosheets on flow-through hollow fiber gas diffusion electrode for high-efficiency CO_2 reduction to formate, Appl. Catal. B 286 (2021) 119945, https://doi.org/10.1016/j.apcatb.2021.119945.

[41] H. Rabiee, L. Ge, X. Zhang, S. Hu, M. Li, S. Smart, Z. Zhu, H. Wang, Z. Yuan, Stand-alone asymmetric hollow fiber gas-diffusion electrodes with distinguished bronze phases for high-efficiency CO_2 electrochemical reduction, Appl. Catal. B 298 (2021) 120538, https://doi.org/10.1016/j.apcatb.2021.120538.

[42] H. Rabiee, X. Zhang, L. Ge, S. Hu, M. Li, S. Smart, Z. Zhu, Z. Yuan, Tuning the Product Selectivity of the Cu Hollow Fiber Gas Diffusion Electrode for Efficient CO_2 Reduction to Formate by Controlled Surface Sn Electrodeposition, ACS Appl. Mater. Interfaces 12 (2020) 21670–21681, https://doi.org/10.1021/acsami.0c03681.

[43] Y. He, Y. Cui, W. Shang, Z. Zhao, P. Tan, Insight into potential oscillation behaviors during Zn electrodeposition: Mechanism and inspiration for rechargeable Zn batteries, Chem. Eng. J. 438 (2022) 135541, https://doi.org/10.1016/j.cej.2022.135541.

[44] W. Luo, Q. Zhang, J. Zhang, E. Moioli, K. Zhao, A. Züttel, Electrochemical reconstruction of ZnO for selective reduction of CO_2 to CO, Appl. Catal. B 273 (2020) 119060, https://doi.org/10.1016/j.apcatb.2020.119060.

[45] A. Gomes, M.I. da Silva Pereira, Pulsed electrodeposition of Zn in the presence of surfactants, Electrochim. Acta 51 (2006) 1342–1350, https://doi.org/10.1016/j.electacta.2005.06.023.

[46] F. Quan, D. Zhong, H. Song, F. Jia, L. Zhang, A highly efficient zinc catalyst for selective electroreduction of carbon dioxide in aqueous NaCl solution, J. Mater. Chem. A 3 (2015) 16409–16413, https://doi.org/10.1039/c5ta04102c.

[47] A. Gomes, M.I. da Silva Pereira, Zn electrodeposition in the presence of surfactants, Electrochim. Acta 52 (2006) 863–871, https://doi.org/10.1016/j.electacta.2006.06.025.

[48] D.L.T. Nguyen, M.S. Jee, D.H. Won, H. Jung, H.-S. Oh, B.K. Min, Y.J. Hwang, Selective CO_2 Reduction on Zinc Electrocatalyst: The Effect of Zinc Oxidation State Induced by Pretreatment Environment, ACS Sustainable Chem. Eng. 5 (2017) 11377–11386, https://doi.org/10.1021/acssuschemeng.7b02460.

[49] R.P.H. Jong, G. Mul, Gas flow Stimulated Hydrodynamics for Preparation and Application of Platinized Titanium Hollow Fibre Electrodes, ChemElectroChem 9 (2022), https://doi.org/10.1002/celc.202101135.

[50] S. Li, X. Dong, Y. Zhao, J. Mao, W. Chen, A. Chen, Y. Song, G. Li, Z. Jiang, W. Wei, Y. Sun, Chloride Ion Adsorption Enables Ampere-Level CO_2 Electroreduction over Silver Hollow Fiber, Angew. Chem. Int. Ed. Engl. 61 (2022) e202210432.